

Coupling of Surface Ocean Heat and Carbon Perturbations over the Subtropical Cells under Twenty-First Century Climate Change

K. B. RODGERS,^{a,b} M. ISHII,^c T. L. FRÖLICHER,^{d,e} S. SCHLUNEGGER,^f O. AUMONT,^g K. TOYAMA,^c
AND R. D. SLATER^f

^a Center for Climate Physics, Institute for Basic Science, Busan, South Korea

^b Pusan National University, Busan, South Korea

^c Oceanography and Geochemistry Research Department, Meteorological Research Institute, Japan Meteorological Agency, Tsukuba, Japan

^d Climate and Environmental Physics, Physics Institute, University of Bern, Bern, Switzerland

^e Oeschger Centre for Climate Change Research, University of Bern, Bern, Switzerland

^f Atmosphere and Ocean Sciences Program, Princeton University, Princeton, New Jersey

^g Sorbonne University, UPMC, University of Paris-06-CNRS-IRD-MNHN, LOCEAN/IPSL, Paris, France

(Manuscript received 31 December 2019, in final form 28 June 2020)


ABSTRACT

It is well established that the ocean plays an important role in absorbing anthropogenic carbon C_{ant} from the atmosphere. Under global warming, Earth system model simulations and theoretical arguments indicate that the capacity of the ocean to absorb C_{ant} will be reduced, with this constituting a positive carbon–climate feedback. Here we apply a suite of sensitivity simulations with a comprehensive Earth system model to demonstrate that the surface waters of the shallow overturning structures (spanning 45°S–45°N) sustain nearly half of the global ocean carbon–climate feedback. The main results reveal a feedback that is initially triggered by warming but that amplifies over time as C_{ant} invasion enhances the sensitivity of surface $p\text{CO}_2$ to further warming, particularly in the warmer season. Importantly, this “heat–carbon feedback” mechanism is distinct from (and significantly weaker than) what one would expect from temperature-controlled solubility perturbations to $p\text{CO}_2$ alone. It finds independent confirmation in an additional perturbation experiment with the same Earth system model. There mechanism denial is applied by disallowing the secular trend in the physical state of the ocean under climate change, while simultaneously allowing the effects of heating to impact sea surface $p\text{CO}_2$ and thereby CO_2 uptake. Reemergence of C_{ant} along the equator within the shallow overturning circulation plays an important role in the heat–carbon feedback, with the decadal renewal time scale for thermocline waters modulating the feedback response. The results here for 45°S–45°N stand in contrast to what is found in the high latitudes, where a clear signature of a broader range of driving mechanisms is present.

1. Introduction

An important priority in climate research is to identify and understand processes that modulate or limit the rate at which the ocean can absorb anthropogenic carbon from the atmosphere under future climate change. Recent analyses demonstrate that over 1959–2017, approximately 25% of anthropogenic carbon emissions were absorbed by the ocean (Friedlingstein et al. 2019),

but perturbations to the ocean state in the future may limit the ocean’s ability to absorb anthropogenic carbon. For the case where anthropogenic perturbations to the ocean state may result in more CO_2 being left in the atmosphere and a resulting radiative heating of the Earth system, we refer to this as a positive climate feedback. There is long-standing interest in how anthropogenic heat entering the ocean can trigger climate feedbacks through reduced ocean CO_2 uptake (Banks and Gregory 2006; Xie and Vallis 2012; Frölicher et al.

 Denotes content that is immediately available upon publication as open access.

Corresponding author: K. B. Rodgers, krodgers@pusan.ac.kr



This article is licensed under a Creative Commons Attribution 4.0 license (<http://creativecommons.org/licenses/by/4.0/>).

DOI: 10.1175/JCLI-D-19-1022.1

© 2020 American Meteorological Society

Unauthenticated | Downloaded 03/01/21 06:36 PM UTC

2015; Winton et al. 2013). To date, these studies have emphasized potential for climate feedbacks through the impact of perturbations on the physical state of the ocean that impact ventilation of heat and carbon anomalies differently.

With the availability of Earth system models, including prognostic ocean biogeochemistry components, a series of related efforts over the past 15 years have focused on developing a framework for quantifying carbon–climate feedbacks. Efforts to identify carbon–climate feedbacks with climate models began with the studies of Maier-Reimer et al. (1996), Sarmiento et al. (1998), and Joos et al. (1999), where the focus was on marine carbon–climate feedbacks. This was subsequently considered by Cramer et al. (2001) for land carbon cycle–climate feedbacks. A now ubiquitous framework for quantifying feedbacks was developed in a series of studies that addressed both marine and land contributions, first by Cox et al. (2000) and then by Friedlingstein et al. (2003, 2006). Although the original studies focused on global diagnostics of feedbacks, subsequent work (an example being the multimodel comparison study of Roy et al. 2011) considered a regional breakdown of where ocean carbon–climate feedbacks find strongest expression. By considering four models that were forced under a Special Report on Emissions Scenarios (SRES) A2 future (2000–2100) scenario (Nakićenović and Swart 2000), the study of Roy et al. (2011) indicated that the low-latitude regions spanned by 44°S–49°N dominate global carbon–climate feedbacks by contributing 71% of the global total when averaged across the models. This is important as it includes neither of the high-latitude regions that were emphasized in the pioneering works of Maier-Reimer et al. (1996) (North Atlantic focus) and Sarmiento et al. (1998) (Southern Ocean focus).

Ocean carbon feedbacks on the climate system under anthropogenic carbon emissions have been addressed historically in two different ways, both addressing how ocean perturbations may result in more CO₂ in the atmosphere than would be expected for an unperturbed ocean state. The first and early framing relates to thermodynamic perturbations to carbon chemistry and the potential impact of CO₂ invasion on the CO₂ buffering capacity of surface waters (Revelle and Suess 1957; Zeebe and Wolf-Gladrow 2001). As the CO₂ buffering capacity decreases with increasing CO₂ invasion, the ocean's ability to absorb CO₂ from the atmosphere relative to an unperturbed ocean state will be diminished, and such feedbacks could in principal occur for an unperturbed (preindustrial) circulation state of the ocean. The second class of feedback mechanisms, developed over subsequent decades, invoke perturbations to the physical circulation state of the ocean, and ensuing perturbations to mixing, biology, and a range of other

consequences. If the upper ocean warms and the surface polar regions freshen, increased stratification reduces the ocean interior ventilation rate. Together with a reduced solubility of CO₂ in warmer waters, it is expected that this would reduce the uptake of CO₂ (Siegenthaler and Oeschger 1978; Maier-Reimer et al. 1996; Sarmiento et al. 1998; Joos et al. 1999; Schwinger and Tjiputra 2018). Within the marine carbon cycle feedback framework that has gained widespread usage in the climate literature (Cox et al. 2000; Friedlingstein et al. 2003, 2006; Roy et al. 2011), Earth system models have been applied to quantify both globally and regionally the degree to which ocean uptake of CO₂ is decreased for a perturbed relative to an unperturbed preindustrial state of the ocean. Although the diagnostics have proven invaluable for the quantification of feedbacks, there is not yet a consensus on the relative contributions of physical drivers (subduction and ventilation), perturbations to biology, and drivers that operate through perturbations to the carbon dioxide buffering capacity of surface waters.

The main objective of this study is to demonstrate that a heat–carbon feedback over the low latitudes (45°S–45°N) is triggered through heating of surface waters, with amplification through time occurring through the cumulative invasion flux of anthropogenic carbon boosting the sensitivity of sea surface *p*CO₂ to warming, with this amplification being larger in the warmer season. This is investigated through a suite of perturbation sensitivity studies with a CMIP5-generation Earth system model, using a high greenhouse gas emissions scenario (historical/RCP8.5) as the baseline for evaluating changes over the period 1861–2100. Although our principal interest is in mechanisms occurring over the low latitudes, we present global diagnostics in order to explore potentially contrasting mechanisms that occur over low and high latitudes in sustaining marine carbon–climate feedbacks.

2. Methods

a. Simulations

Here we apply a suite of five simulations with the Geophysical Fluid Dynamics Laboratory (GFDL) Earth system model (ESM2M; Dunne et al. 2012, 2013) under historical and future atmospheric CO₂ concentration pathways. The physical state model underlying ESM2M is an updated version of GFDL's coupled model CM2.1 (Delworth et al. 2006). The ocean component is version 4.1 of the Modular Ocean Model (MOM4p1) (Griffies 2009) with approximately 1° horizontal resolution in the ocean that is enhanced meridionally near the equator and with 50 vertical layers. The

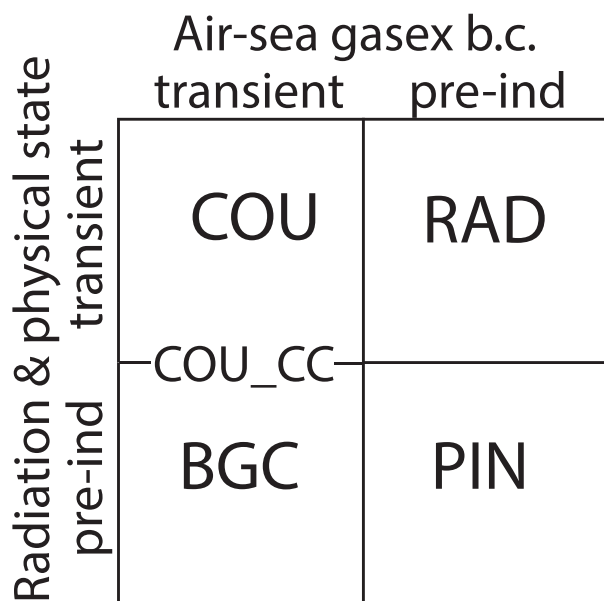


FIG. 1. Schematic for five model runs considered here, following the nomenclature of Gregory et al. (2009). The fully coupled case is denoted COU, the radiatively coupled case is denoted RAD, the biogeochemically coupled case is denoted BGC, and the preindustrial run is denoted PIN. An additional run is introduced in our analysis here, namely COU_CC (COU with constant climate, namely a preindustrial circulation state). For COU_CC the circulation state of the ocean is that shared by the PIN and BGC, but data override with the daily SST and SSS fields from the COU run used to calculate $p\text{CO}_2$ for COU_CC within the gas exchange routines. As such, COU_CC should be interpreted as being analogous to the COU case except with mechanism denial in terms of not allowing a transient in the circulation state.

atmospheric component of ESM2M is AM2 (Anderson et al. 2004), with approximately 2° horizontal resolution in the atmosphere. The ocean biogeochemical model is Tracers of Ocean Phytoplankton and Allometric Zooplankton code, version 2 (TOPAZv2), including 30 tracers to represent cycles of carbon, oxygen, the major macronutrients, and iron (Dunne et al. 2010). The fidelity of ESM2M to observational constraints over the historical period has been addressed by Dunne et al. (2012, 2013), and the small transient climate response (TCR) of ESM2M relative to the CMIP5 models has been described by Forster et al. (2013). The fidelity of ESM2M in simulating ocean uptake of anthropogenic carbon has been described in the study of Frölicher et al. (2015).

The experimental design underlying this study is intended to deconvolve the relative contributions of thermodynamics of marine carbon chemistry and ventilation rate changes (ocean physics) and biological perturbations in sustaining marine carbon–climate feedbacks. Five simulations are organized to interpret

feedbacks on the fully coupled simulation (COU) that follows a historical/RCP8.5 pathway over 1861–2100 (van Vuuren et al. 2011) (Fig. 1). The simulations apply prescribed mixing ratios for atmospheric CO_2 and other non- CO_2 radiative forcing agents. The first principal simulation (COU) uses the historical/RCP8.5 CO_2 boundary conditions for radiative as well as for the land and ocean biogeochemistry components. The second simulation [biogeochemically coupled (BGC)] is the same as the COU simulation, except the concentrations of greenhouse gases and other radiative agents were kept at preindustrial levels in the radiation code, while atmospheric CO_2 concentrations follow the historical/RCP8.5 pathway in the gas exchange code. Conversely, the third simulation [radiatively coupled (RAD)] includes the increase of greenhouse gases and their radiative agents on the physical state of the climate system with associated perturbations to the global carbon cycle, but for air–sea gas exchange the ocean sees a persistent preindustrial mixing ratio for atmospheric CO_2 . We also included a control simulation under preindustrial conditions (PIN), with this consisting of a 240-yr extension of the original spinup run.

An additional simulation, COU constant circulation (COU_CC), was performed using precisely the same physical state evolution as was used for BGC over the corresponding period 1861–2100 (a preindustrial ocean state), but the thermodynamic terms impacting sea surface $p\text{CO}_2$ used for gas exchange were calculated using high-frequency output from the COU run for which there are important climate transients in surface temperature and salinity. This was accomplished by first saving daily mean SST and SSS from the COU simulation over the full interval 1861–2100. These daily mean SST and SSS fields were then read into the gas exchange routines for the calculation of $p\text{CO}_2$ in the COU_CC simulation, and linearly interpolated to the (2h) time step of the ocean model, thereby impacting gas exchange at the sea surface through their impact on $\Delta p\text{CO}_2$. The other terms required in the calculation of $p\text{CO}_2$ at the surface in the COU_CC simulation, namely surface dissolved inorganic carbon, surface alkalinity, PO_4 , and SiO_4 , were taken directly from the fully prognostic fields in the biogeochemistry model (TOPAZ) in the COU_CC simulation.

In this way, the CO_2 system in surface seawater (including the buffering capacity) for the new COU_CC run feels the warming transient, but COU_CC is not impacted by the changes in stratification and ventilation rates/pathways experienced by the COU run itself. Specifically in the CO_2 chemistry calculations (Mehrbach et al. 1973; Najjar and Orr 1999), K_0 (the solubility constant) is perturbed through the effects of temperature and

salinity, as are K_1 and K_2 (dissociation constants of carbonic acid). Thus, the COU_CC perturbation experiment is best understood as being a COU analog, where through mechanism denial the transient in the ventilation rate for the ocean has been disallowed. It is important to keep in mind that the cumulative effect of the perturbation applied in COU_CC results in reduced global carbon uptake relative to BGC (the unperturbed case). It is also worth noting that we chose to build COU_CC on the preindustrial circulation state of BGC with targeted perturbation to SST and SSS in the gas exchange routines, rather than the reverse configuration building on a transient circulation state with targeted SST and SSS perturbations from a preindustrial state of the model. Our choice was motivated by the view that the results based on a preindustrial circulation state would be much more straightforward to interpret.

b. Data-based sea surface $p\text{CO}_2$ products

Our primary analysis here focuses on model projections, but we also make use of observational products to assess the fidelity of ESM2M in several regions of interest. We utilize two databased $p\text{CO}_2$ products: The Princeton University Markov chain Monte Carlo (PU-MCMC) method (Majkut et al. 2014) and the product of the Japan Meteorological Agency (JMA) (Iida et al. 2015). To represent the evolution of $p\text{CO}_2$ in SST–salinity-normalized dissolved inorganic carbon (nDIC) space for the observational products PU-MCMC and JMA, it is necessary to specify a second variable in the carbonate system of seawater to derive DIC. We have chosen here to use two published empirical methods for calculating alkalinity to this end. For the two Pacific sites [the formation region for North Pacific Subtropical Mode Water (NPSTMW) and the equatorial Pacific divergence region (EQDIV)], we use the interannually varying monthly climatology of Takatani et al. (2014), and for the subpolar North Atlantic we use the product of Lee et al. (2006) [the method of Takatani et al. (2014) has not yet been extended to include the Atlantic]. As was presented in the study of Takatani et al. (2014), incorporating remotely sensed sea surface height variations in an empirically based account of surface alkalinity offers a number of distinct advantages over the method of Lee et al. (2006), in particular in regions such as NPSTMW that are on the poleward flank of the subtropical gyres. To maintain consistency with the observational products used to derive the product of Takatani et al. (2014), we also use sea surface salinity from the product of Usui et al. (2006) and the sea surface temperature product of Kurihara et al. (2006) in calculating nDIC over the 2000s, and subsequently for the construction of a climatology over the same period.

Likewise, the same temperature and salinity fields are provided for the North Atlantic to the calculation of alkalinity using the method of Lee et al. (2006). To facilitate comparison, the figures normalize all fields to constant alkalinity and salinity values that are given in the figure panels (this will be shown in Figs. 5 and 6). All of the CO_2 chemistry calculations are performed using the method of Lueker et al. (2000), as are the isolines of constant $p\text{CO}_2$ in each of the panels.

c. Diagnostics of the changes in the CO_2 buffering capacity of surface waters

Additionally, we consider the Revelle factor (Revelle and Suess 1957) as a diagnostic of the buffering capacity of CO_2 in surface seawater, with this commonly expressed with

$$\text{Revelle factor} = (\Delta p\text{CO}_2/p\text{CO}_2)/(\Delta\text{DIC}/\text{DIC}).$$

For the calculations used here, we employ the CO2SYS algorithms of van Heuven et al. (2011), to which we first calculate the monthly mean Revelle factor using DIC concentrations, in conjunction with SST and SSS ($p\text{CO}_2$ is also required for the iterative calculations performed offline with CO2SYS).

3. Results

We begin by considering the integrated air–sea CO_2 fluxes over the period 1861–2100 for the different simulations and regions (Fig. 2). The global ocean CO_2 uptake for the COU case (black solid line in Fig. 2a) is reduced by 1.3 PgC yr^{-1} during the 2090s in comparison with the BGC case (green line in Fig. 2a), indicating the well-known positive global carbon–climate feedback, with the contrast between COU and BGC being larger than the contrast between RAD (red line in Fig. 2a) and PIN (blue line in Fig. 2a) of 0.19 PgC yr^{-1} . This non-linearity has previously been discussed in the studies of Gregory et al. (2009) and Schwinger et al. (2014).

We next consider integrated CO_2 uptake over three distinct latitude bands of the global domain. Given our primary interest in CO_2 uptake over the shallow overturning cells (encompassing thermocline and subpolar mode waters) spanning 45°S – 45°N (Iudicone et al. 2016; Toyama et al. 2017), we divide the global domain into three bands. These are 45°S – 45°N (shallow overturning), 45° – 90°N (northern high latitudes), and 90° – 45°S (southern high latitudes). A comparison over the three latitude bands reveals that 60% of the global cumulative carbon uptake occurs within the low latitudes (45°S – 45°N) by the end of the twenty-first century (Figs. 2b,c). In fact, this dominance of thermocline density-class waters in uptake

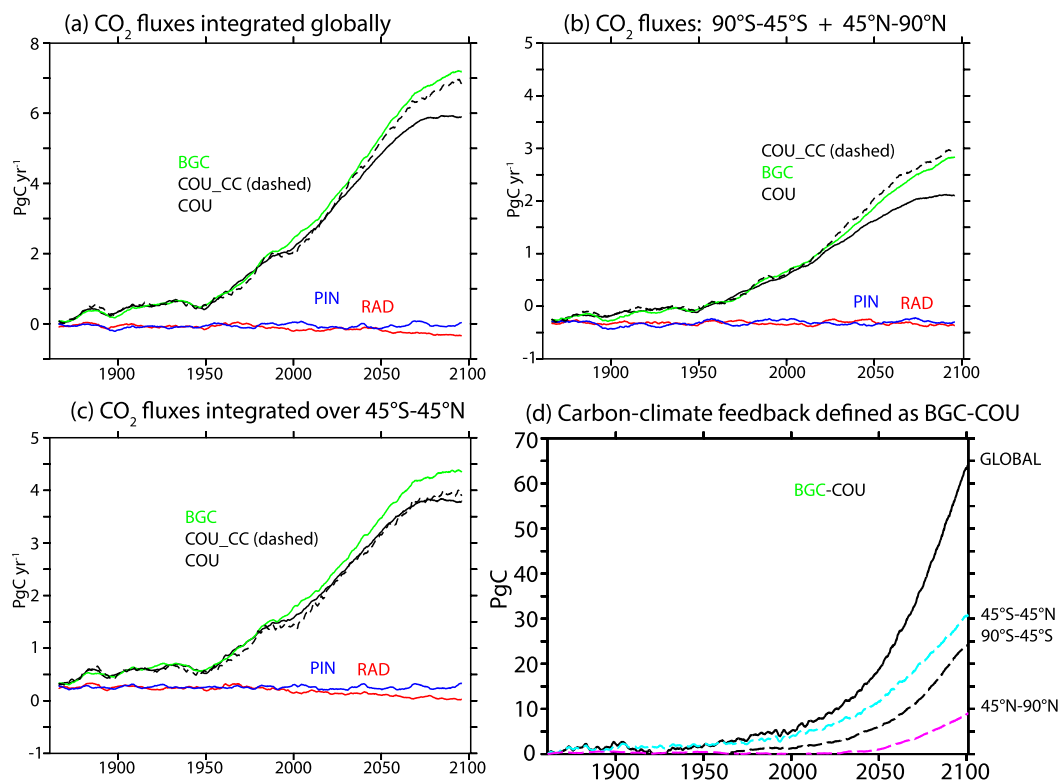


FIG. 2. For ESM2M over 1861–2100, (a) globally integrated uptake for COU, RAD, BGC, PIN, and COU_CC cases as defined in Fig. 1b combined uptake integrated over both (b) the high northern latitudes 45°S–45°N and the Southern Ocean defined as the region 90°–45°S, and (c) uptake integrated over 45°S–45°N. (d) The differences in the cumulative uptake for BGC and COU globally and by latitude range.

is not surprising considering that the latitudes 45°S–45°N span 82% of the global ocean surface area. The regions spanning 90°–45°S and 45°–90°N absorb approximately 30% and 10% of the global total, respectively.

Importantly, the spatially integrated CO₂ fluxes for COU_CC over 45°S–45°N (dashed line in Fig. 2c) reveals that surface warming in conjunction with the invasion flux of CO₂ is able to drive nearly all of the carbon–climate feedback over this region. Thus, the large-scale reduction in CO₂ uptake over 45°S–45°N for COU relative to BGC is first triggered by surface heating, and then amplified in time by the invasion flux of anthropogenic CO₂ boosting the sensitivity of surface temperature perturbations. In other words, the underlying driver of changes in *p*CO₂ are SST rather than DIC or alkalinity (ALK) driven. This stands in contrast to the higher latitudes of both hemispheres (Fig. 2b), where perturbations to the ocean circulation state under climate change sustain important changes to the natural carbon cycle and clearly to *p*CO₂ (DIC-driven changes) (de Lavergne et al. 2014; Winton et al. 2013).

The reduction in cumulative anthropogenic carbon uptake due to climate change (differences between the

COU and BGC simulations) over 1861–2100 is investigated next. Cumulative carbon uptake is reduced by 10% (567 PgC in COU vs 632 PgC in BGC, with a total perturbation of 64.2 PgC) due to climate change by 2100 (black line in Fig. 2d). The low latitudes contribute 48% (31 PgC) to the global difference, whereas 90°–45°S and 45°–90°N contribute only 38% (24 PgC) and 14% (9 PgC), respectively (Fig. 2d). Although the contribution of the Southern Ocean is larger per unit area than the latitudes spanned by the shallow overturning, the vast expanse of the region spanning 45°S–45°N allows this region to contribute nearly half of the global total. Over global scales, it warrants mention that by 2095, the large ensemble suite of 30 runs with ESM2M (Rodgers et al. 2015), identical in their forcing and model configuration to the COU run here, differ in their global total DIC inventories with a standard deviation of 1.2 PgC, with this being only 2% of the 64.2 PgC difference in global total DIC inventories for BGC and COU. This confirms that the difference in total DIC inventories between BGC and COU unambiguously represents an emerged response to the applied perturbation, rather than reflecting differences associated with natural variability.

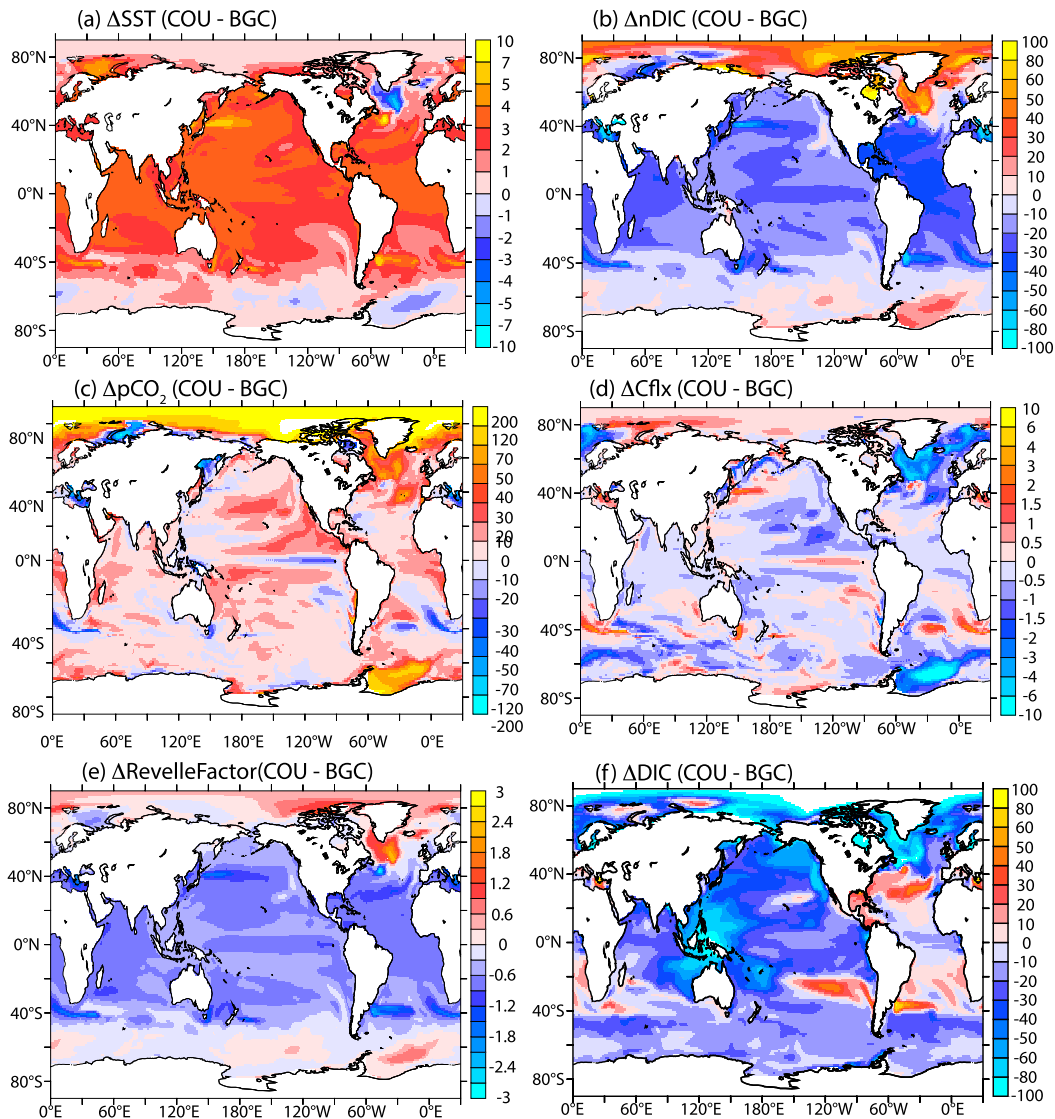


FIG. 3. Maps showing annual mean perturbation structures, averaged over the 20-yr intervals 2080–99. The fields shown are (a) difference in sea surface temperature ($^{\circ}\text{C}$) between COU and BGC; (b) difference in sea surface nDIC ($\mu\text{mol kg}^{-1}$) for COU and BGC runs; (c) difference in $p\text{CO}_2$ (μatm) between COU and BGC; (d) difference in sea–air CO_2 flux ($\text{molC m}^{-2} \text{yr}^{-1}$) between COU and BGC; (e) the change in the surface ocean Revelle factor between COU and BGC; (f) difference in sea surface DIC ($\mu\text{mol kg}^{-1}$) for COU and BGC runs.

To gain insight into the mechanistic controls on carbon–climate feedbacks for our three regions of interest, we turn our attention to the annual mean perturbations for COU relative to BGC (considered as averages over 2080–99) for SST (Fig. 3a), nDIC (Fig. 3b), $p\text{CO}_2$ (Fig. 3c), CO_2 fluxes (Fig. 3d), changes in the surface ocean Revelle factor (Fig. 3e), and finally changes in surface ocean DIC concentrations (Fig. 3f). SST perturbations in ESM2M are characterized by broad warming over most of 40°S – 70°N , with relatively weak temperature responses over the Southern Ocean and subpolar North Atlantic that even includes cooling

in places. nDIC is reduced under warming over much of the low latitudes but on average is larger over much of the Southern Ocean and also over the subpolar North Atlantic and Arctic. There is a strong correspondence between the patterns of SST and nDIC perturbations, with the area-weighted Spearman rank coefficient for the annual mean of both fields is 0.74. Globally, the average change in sea surface nDIC concentrations is -5.5% ($-8.3 \mu\text{mol kg}^{-1} \text{C}^{-1}$). The average change over 45°S – 45°N is -8.0% , over 90°S – 45°S it is $+1.8\%$, and over 45°S – 45°N the average change in surface nDIC is very similar to the net

reduction in cumulative uptake over 45°S–45°N through air–sea fluxes (−8.3%). The evolution of CO₂ fluxes integrated over 45°S–45°N in Fig. 2c is consistent with the interpretation that SST-driven decreases in the solubility of CO₂ of surface waters [$K_0 = \text{CO}_2(\text{aq})/p\text{CO}_2$] as well as through perturbations to the dissociation constants for carbonic acid K_1 and K_2 (and thereby reflected in decreased nDIC) sustain decreased uptake of CO₂ for the warming case (COU) relative to the case without warming (BGC).

Positive changes in $p\text{CO}_2$ between COU and BGC (Fig. 3c) indicate a reduced thermodynamic gradient of $p\text{CO}_2$ into the ocean from the atmosphere. Aside from the Arctic, large positive $p\text{CO}_2$ changes are found in the subpolar North Atlantic and the Weddell Sea (Fig. 3c), with these changes reflected in globally maximum decreases in CO₂ uptake for the same regions (Fig. 3d). However, over most of 45°S–45°N, there is a smaller but widespread reduction in CO₂ uptake for COU relative to BGC, with exceptions being the equatorial Pacific upwelling regions and the regions spanning the Agulhas, the South Atlantic, and the Arctic.

In contrast to the spatially smoothly varying perturbation patterns for nDIC over the latitudes 45°S–45°N (Fig. 3b), the perturbation patterns for $p\text{CO}_2$ (Fig. 3c) and CO₂ fluxes (Fig. 3d) for COU relative to BGC reveal significantly more spatial structure. In fact, the eastern equatorial Pacific upwelling region exhibits locally enhanced uptake via gas exchange for COU relative to BGC, despite the fact that nDIC is reduced for this same upwelling region. For the case of the equatorial Pacific, this reflects the signature of re-emergence of higher anthropogenic carbon concentrations for BGC relative to COU (Toyama et al. 2017; Zhai et al. 2017), with the meridional width of this extremum near the equator related to the air–sea equilibration time scale.

We consider in Fig. 3e the perturbation to the surface ocean Revelle factor (Revelle and Suess 1957) for the difference between COU and BGC averaged over 2080–99. Clearly the Revelle factor perturbations over large scales largely reflect the nDIC perturbations (Fig. 3b), with this in turn reflecting the SST perturbations (Fig. 3a). To emphasize the insight provided through nDIC, we also consider the change in DIC itself (Fig. 3f), where the differences between COU and BGC show significantly less correlation to the pattern of SST perturbations (Fig. 3a) than nDIC (Fig. 3b) due to the signature of freshwater perturbations under climate change on surface DIC concentrations.

What is particularly instructive about the differences shown in Fig. 3 is that COU exhibits higher sea surface

$p\text{CO}_2$ and absorbs less CO₂ from the atmosphere over 45°S–45°N, despite COU having lower nDIC and DIC concentrations than BGC. Although this may appear at first to be counterintuitive, we wish to emphasize here that it is the much higher DIC and thus $p\text{CO}_2$ for COU relative to PIN that enhances the sensitivity of $p\text{CO}_2$ to temperature changes, and thereby sustains the differences in CO₂ uptake over 45°S–45°N between COU and BGC. Likewise, it may seem counterintuitive that the Revelle factor is lower for COU than for BGC (Fig. 3e), while CO₂ uptake is less than COU relative to BGC (Fig. 3d). There as well, it is the impact of the much larger changes in DIC for COU relative to PIN that sustain the heat–carbon feedback mechanism. Whereas the perturbation to the Revelle factor averaged over 45°S–45°N between COU and BGC (Fig. 3e) is −0.6, the Revelle factor perturbation over the same region between COU and PIN is 4.0, with this being more than a factor of 6 larger in terms of absolute amplitude.

Our analysis in Fig. 3 focused on decadal mean perturbations for the model. Next, we turn our attention to seasonal variations in air–sea CO₂ fluxes and $p\text{CO}_2$. Our interest is in the subtropical regions, and we begin in Fig. 4a with the example of monthly mean CO₂ fluxes integrated over 15°–45°N for the COU (black lines) and in Fig. 4b with monthly mean CO₂ fluxes integrated over the same region for BGC. For both cases, the seasonal cycle in CO₂ fluxes increases with time (consistent with Rodgers et al. 2008), with this increase being larger for COU than for BGC. To focus on the structure of the seasonal cycle at the end of the twenty-first century, we show next climatological fluxes over 2080–99 for 15°–45°N in Fig. 4c (COU shown in black; BGC shown in red). For this latitude range, there is a seasonal asymmetry in the amplification of amplitude for COU relative to BGC, with the amplitude perturbation being larger in late summer than during other parts of the seasonal cycle. Viewing BGC as a neutral state against which COU represents a perturbation, this clearly reveals that perturbations that are not evenly distributed over the seasonal cycle are sustaining the decreased uptake of COU relative to BGC of $\sim 0.2 \text{ PgC yr}^{-1}$ averaged over 2080–99.

For the latitude band 45°–15°S (Fig. 4d) the case of COU also reveals perturbations to the seasonal cycle of the neutral state BGC, with COU having $\sim 0.1 \text{ PgC yr}^{-1}$ less uptake over this latitude band averaged over the period 2080–99 than BGC. Once again, the difference between COU and BGC is not evenly distributed over the seasonal cycle. To get a foothold on the spatial structures over which this occurs, we consider for the North Pacific (the subtropical region with the largest signal) the late-summer $\Delta p\text{CO}_2$ (ocean minus

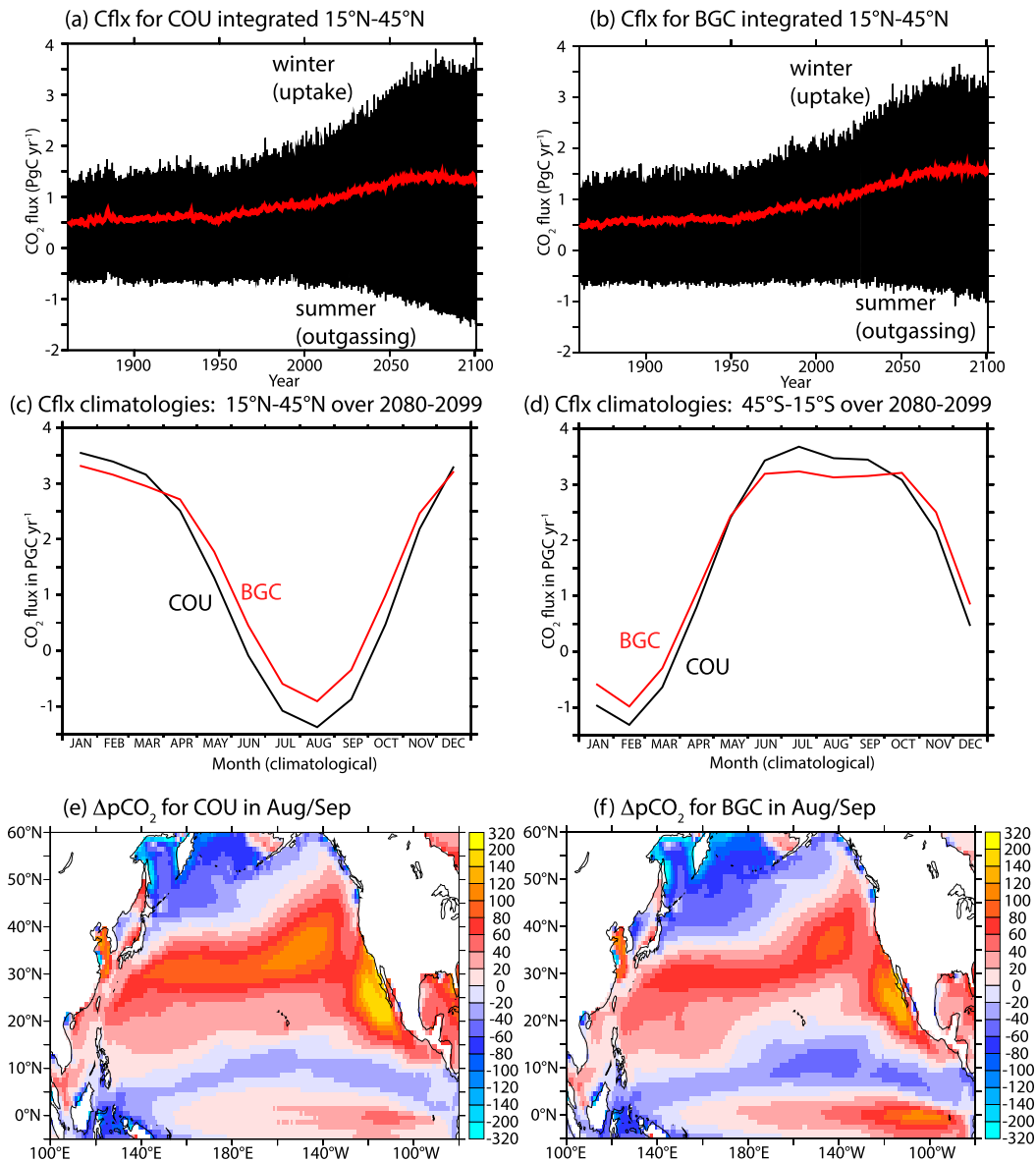


FIG. 4. (a) Air–sea CO_2 fluxes for COU (PgC yr^{-1} ; positive values indicate uptake by the ocean) integrated over $15^\circ\text{--}45^\circ\text{N}$ for monthly mean (black lines) and annual mean (red line); (b) air–sea CO_2 fluxes (PgC yr^{-1}) for BGC integrated over $15^\circ\text{--}45^\circ\text{N}$ for COU; (c) seasonal climatology of air–sea CO_2 fluxes (PgC yr^{-1}) integrated over $15^\circ\text{--}45^\circ\text{N}$ over 2080–99 for COU (black line) and BGC (red line); (d) seasonal climatology of CO_2 fluxes (PgC yr^{-1}) integrated over $45^\circ\text{--}15^\circ\text{S}$ over 2080–99; (e) $\Delta p\text{CO}_2$ (μatm) for COU (ocean minus atmosphere) climatological average of August and September for the period 2080–99; (f) $\Delta p\text{CO}_2$ (μatm) for BGC (ocean minus atmosphere) climatological average of August and September for the period 2080–99.

atmospheric $p\text{CO}_2$) averaged over August and September for COU (Fig. 4e) and BGC (Fig. 4f), both considered for climatologies constructed over 2080–99. Diagnostics of the piston velocities used for CO_2 gas exchange reveal that for COU they are only 2% smaller than for BGC over $45^\circ\text{S--}45^\circ\text{N}$, implying that CO_2 uptake differences are dominated by surface ocean $p\text{CO}_2$ differences. The $\Delta p\text{CO}_2$ patterns reveal that the thermodynamic gradient sustaining

outgassing is significantly larger in its maximum in the subtropics and also characterized by a broader meridional structure for COU relative to BGC.

Next we consider the simulated seasonal evolution during the 2090s of $p\text{CO}_2$ within a phase space of SST and nDIC [analogous to that was presented in Fig. A1 of Nakano et al. (2015) and Fig. 5a of Schlunegger et al. (2019)] for the following four regions: 1) the formation

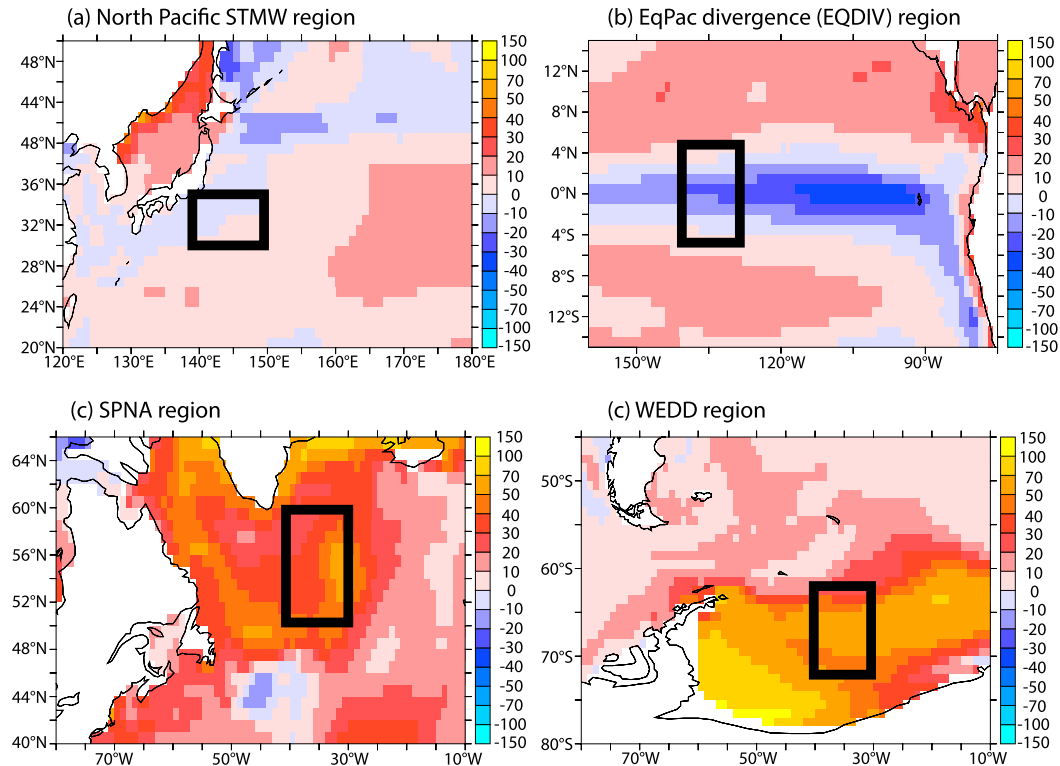


FIG. 5. Definition of regions, with averaging regions denoted with a black box, superposed on the simulated annual mean difference in $p\text{CO}_2$ (COU minus BGC) averaged over 2080–99 (a) NPSTMW (140° – 160°E , 30° – 35°N), (b) EQDIV (140° – 130°W , 5°S – 5°N), (c) SPNA (40° – 30°W , 50° – 60°N), and (d) WEDD (40° – 30°W , 62° – 72°S).

region for NPSTMW (140° – 160°E , 30° – 35°N), 2) EQDIV (140° – 130°W , 5°S – 5°N), 3) the subpolar North Atlantic (SPNA) (40° – 30°W , 50° – 60°N), and 4) the Weddell Sea region of the Southern Ocean (WEDD) (40° – 30°W , 62° – 72°S). These regions are denoted with the bold black box in the four panels of Fig. 5. Representing the full seasonal evolution of $p\text{CO}_2$ allows us to assess the degree to which carbon–climate feedbacks are active in winter versus summer months, or whether they find expression over the full seasonal cycle. The first two of these (NPSTMW and EQDIV) lie within the latitudes spanned by the subtropical cells (45°S – 45°N), whereas the other two regions (WEDD and SPNA) are important in the model for CO_2 exchange with the deeper ocean. (A comparison for the same locations against observational constraints for the 2000s is shown in Fig. 8.)

In the NPSTMW region, each of the four simulations (COU, RAD, BGC, and PIN) presents a similar evolution of the seasonal cycle in $p\text{CO}_2$ in its absolute variations for SST and nDIC (Fig. 6a). COU_CC is not shown for the sake of clarity, as it closely resembles the case of COU. The annual mean nDIC offset between BGC and PIN is $238 \mu\text{mol kg}^{-1}$, and between BGC and COU it is

$13 \mu\text{mol kg}^{-1}$. This decrease in nDIC for COU relative to BGC occurs within the context of an annual mean increase of SST of 2.3°C , and a decrease in salinity and salinity-normalized total alkalinity of 0.25 psu and $2 \mu\text{mol kg}^{-1}$, respectively, for COU relative to BGC. Importantly, the effect of salinity and nALK changes on $p\text{CO}_2$ is very small, and the offset between COU and BGC in SST–nDIC phase space occurs largely parallel to isolines of constant $p\text{CO}_2$, albeit with the annual mean $p\text{CO}_2$ for COU being $11 \mu\text{atm}$ higher than that of BGC, with this being only 2% of the total change in $p\text{CO}_2$ between BGC and PIN of $567 \mu\text{atm}$. We have seen with the case of COU_CC (Fig. 2c) that over the large scales of the subtropical cells the surface carbon cycle response in COU relative to BGC is largely due to SST perturbations. Viewed locally for STMW, Fig. 6a reveals that the amplitude of the nDIC response is approximately $6 \mu\text{mol kg}^{-1}\text{C}^{-1}$, with this being the approximate slope of the constant $p\text{CO}_2$ isolines shown in Fig. 6a. It is important to emphasize that although nDIC decreases by 5.3%, $p\text{CO}_2$ increases by 2.0%. Importantly, this response in a formation region for interior thermocline waters is smaller than the $\sim 8\%$ increase one would

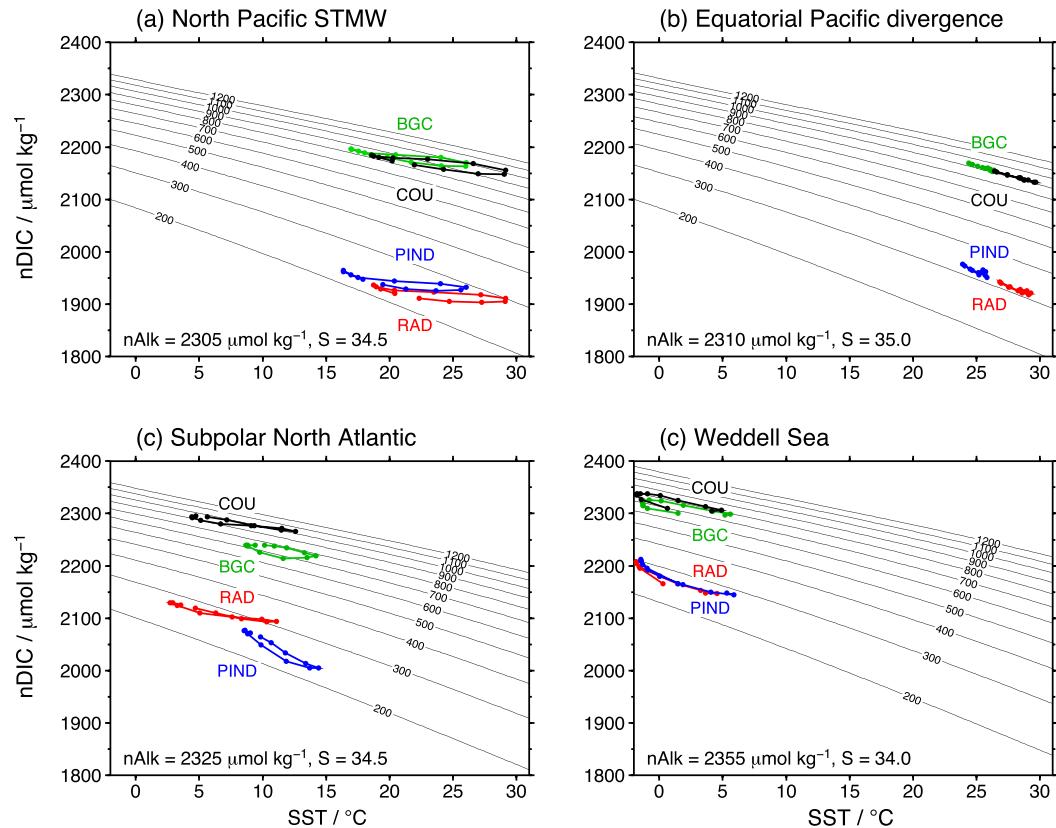


FIG. 6. Phase diagram in SST–nDIC space showing climatological monthly evolution of $p\text{CO}_2$ during the 2090s of COU, BGC, RAD, and PIN runs as defined in Fig. 1 with ESM2M, for the regions highlighted in Fig. 4, namely, (a) NPSTMW, (b) EQDIV, (c) SPNA, and (d) WEDD. The figure uses K_0 from Weiss (1974) and K_1 and K_2 from Lueker et al. (2000).

expect from SST-driven increases in $p\text{CO}_2$ in surface waters (the 4% $p\text{CO}_2$ increase per degree Celsius warming described by Weiss et al. 1982).

Next, we consider the case of EQDIV (Fig. 6b) for the 2090s, corresponding to the narrow strip of upwelling with 5° latitude of the equator between 140° and 130°W . We have chosen to consider the EQDIV region as it offers a perturbation outgassing signature, thus being anomalous from the perturbation $p\text{CO}_2$ and CO_2 fluxes, while nevertheless being consistent with the broader nDIC perturbations occurring over the Pacific subtropical cells. We present analysis for a box with relatively narrow zonal extent to avoid the substantial zonal gradients in the broader Niño-3 box (150° – 90°W , 5°S – 5°N), although the results considered here apply more generally for the region. Importantly, by focusing on a relatively narrow region, we target the upwelling zone for a midthermocline density class from the equatorial undercurrent.

The changes in annual mean $p\text{CO}_2$ between COU and BGC are very small ($-5 \mu\text{atm}$ for EQDIV, as the annual

mean local changes in nDIC ($-19 \mu\text{mol kg}^{-1}$) nearly compensate the annual mean changes in temperature ($+2.7^\circ\text{C}$), while changes in salinity (-0.05psu) and nALK ($-1 \mu\text{mol kg}^{-1}$) have very small impacts. This near compensation in nDIC is reflected in a $p\text{CO}_2$ perturbation that is only -0.9% (a CO_2 ingassing perturbation) as large as the perturbation in $p\text{CO}_2$ for BGC relative to PIN for this same region in the 2090s, with the COU – BGC $p\text{CO}_2$ perturbation of -0.9% also being an order of magnitude smaller than what one would expect from thermodynamic temperature effects on $p\text{CO}_2$. The equatorial Pacific upwelling region maintains a weak equatorial Pacific outgassing signature for both COU and BGC in the 2090s, but modestly weaker for COU. We interpret the lower nDIC concentrations for COU relative to BGC within the EQDIV region to not reflect reduced local uptake of CO_2 from the atmosphere, but rather to reflect differences in thermocline nDIC of recently upwelled waters along the equator. This is deduced from the existence of air–sea equilibration time scales in this region that exceed the residence time of surface

waters in the EQDIV region. We interpret the reduced nDIC for COU relative to BGC in EQDIV to reflect rather differences in preformed nDIC in the extratropical source regions where thermocline waters form at the surface.

For the case of SPNA (Fig. 6c), nDIC is substantially higher for COU than it is for BGC. Consequently, $p\text{CO}_2$ is considerably higher ($45 \mu\text{atm}$) for the COU case than for the BGC case over the full seasonal cycle, despite the compensating changes in SST (-3.2°C), salinity (-1.91 psu), and nALK ($+17 \mu\text{mol kg}^{-1}$). These changes can be attributed to large-scale differences in the physical state of the ocean, and the response in biological processes in the ocean. As such, these changes are intrinsically linked to perturbations of the natural carbon cycle. This is followed by an analysis of the seasonal evolution in SST–nDIC space for $p\text{CO}_2$ for the case of WEDD (Fig. 6d). For COU considered as a perturbation to BGC, both nDIC and $p\text{CO}_2$ are higher ($13 \mu\text{mol kg}^{-1}$ and $44 \mu\text{atm}$, respectively) with the increase in $p\text{CO}_2$ constituting a positive carbon–climate feedback. SST is cooler (-0.5°C) for COU relative to BGC, with this being most pronounced in summer, reflecting reduced convection in this region under global warming (Manabe et al. 1991). From this analysis we see that temperature perturbations that compensate for nDIC as well as salinity (-0.38 psu) and nALK ($+1 \mu\text{mol kg}^{-1}$) are relatively minor. The perturbations to nDIC that drive the $p\text{CO}_2$ perturbations are largest in late austral winter (September).

Taken together, our analysis emphasizes the contrast between two regions within 45°S – 45°N in the Pacific (Figs. 6a,b) and the two high-latitude regions (Figs. 6c,d). The high-latitude regions exhibit strong perturbations in the natural carbon cycle, associated with changes in circulation and/or biology, consistent with behavior seen in previous modeling studies (Sarmiento et al. 1998; Winton et al. 2013; de Lavergne et al. 2014). For both high-latitude sites, nDIC increases for COU relative to BGC despite decreasing in temperature, implicating mixing and/or biological changes that perturb nDIC. The two sites within 45°S – 45°N , on the other hand, are characterized by surface nDIC perturbations that are to first order driven by temperature perturbations, with gas exchange playing an important supporting role. The relatively structured $p\text{CO}_2$ perturbation field shown in Fig. 3c represents the interplay of spatial variations of the slope of $p\text{CO}_2$ lines in SST–nDIC space for the different regions of the surface ocean between COU and BGC.

We have identified broadscale reductions in response to surface warming of both sea surface nDIC and cumulative CO_2 uptake over 45°S – 45°N (both by $\sim 8\%$) by the end of the twenty-first century. The relatively

smooth distribution of nDIC differences (Fig. 3b) over the equatorial upwelling region indicates that re-emerged equatorial thermocline waters have nDIC and thermal perturbations that reflect those of the overlying surface waters. This is consistent with thermocline waters more generally having nDIC concentrations that are reduced by 8% due to heating perturbations to surface waters, in particular for the Eastern Subtropical Mode Water (ESTMW) formation regions thought to be important as a source of Equatorial Undercurrent (EUC) waters (Rodgers et al. 2003; Goodman et al. 2005). The fact that $p\text{CO}_2$ displacements for the EQDIV region in Fig. 6b between BGC and COU fall nearly along a constant $p\text{CO}_2$ isoline reflects large-scale shallow overturning processes (Nakano et al. 2015; Toyama et al. 2017; Zhai et al. 2017) rather than simply local processes in the equatorial divergence region. These results are consistent with the observationally based analysis of Fine et al. (2001) that revealed a decadal-scale shallow overturning time scale for thermocline waters.

By establishing over the region 45°S – 45°N a specific mechanistic coupling between temperature and carbon, our results provide a mechanistic underpinning of the γ_{oc} factor (γ_{oc} being the carbon–climate feedback diagnostic of Friedlingstein et al. (2003), for the reduction in cumulative CO_2 uptake per degree Celsius warming). Importantly, the framework of invoking SST–nDIC phase space to interpret perturbations (Fig. 6), in conjunction with our earlier analysis in Figs. 3 and 4, has allowed us to identify that the feedback over 45°S – 45°N is triggered by surface heating, and subsequently the sensitivity of surface $p\text{CO}_2$ to temperature perturbations is amplified in time through the invasion flux of anthropogenic carbon (taken as COU minus PIN), in particular during the warm season. Importantly, Fig. 6 also confirms that biological perturbations are not important players in sustaining the differences in CO_2 uptake between COU and BGC over 45°S – 45°N .

The details of the fields used to identify γ_{oc} by Friedlingstein et al. (2003) are not equivalent to the local relationship we identified in Fig. 6 between SST and nDIC. Thus we are motivated to consider over the expanse 45°S – 45°N the relationship between the SST perturbations (COU minus BGC) over this region with the perturbation to cumulative CO_2 uptake over this region (COU minus BGC) in Fig. 7a (analogous to Fig. 2d in Friedlingstein et al. 2006). For this analysis 10-yr means of both fields over 1861–2100 were used. As temperatures over 45°S – 45°N increase, there is a corresponding decrease in CO_2 uptake for COU relative to BGC. The response of cumulative CO_2 uptake to warming is relatively weak until approximately the year 2000, with an abrupt change to a stronger sensitivity over the twenty-first

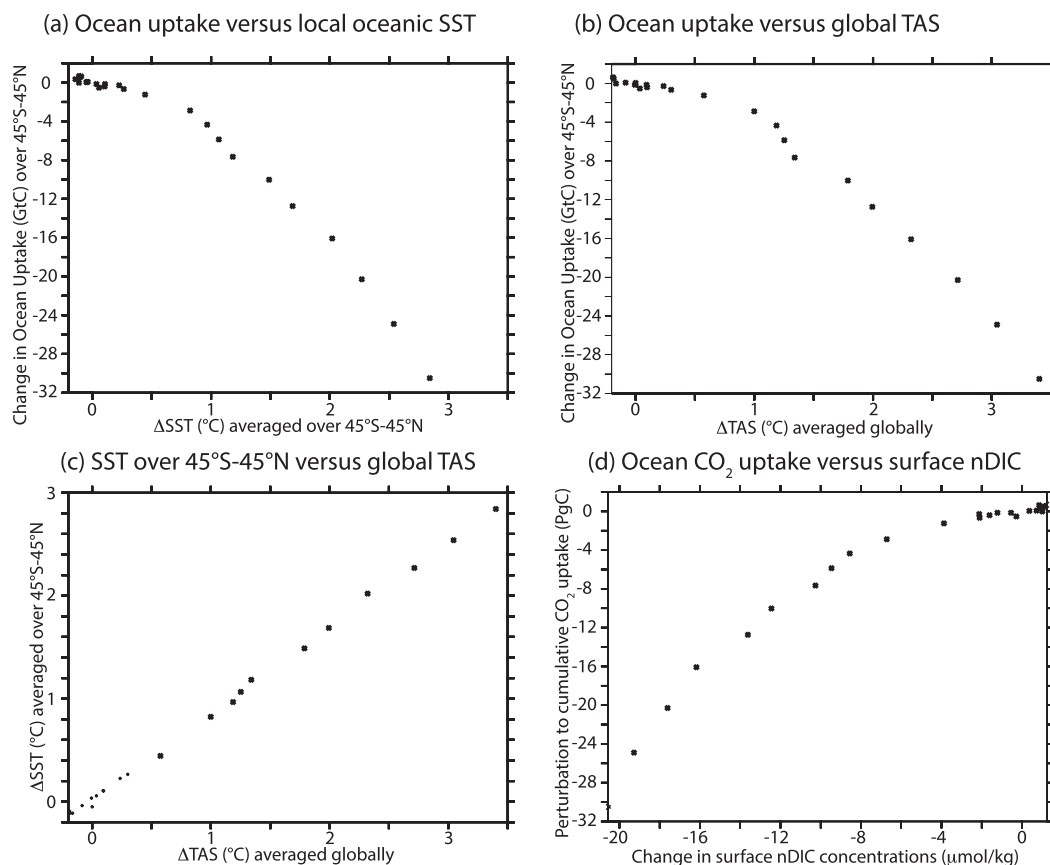


FIG. 7. (a) Relationship between perturbations to SST perturbations ($^{\circ}\text{C}$) averaged over 45°S – 45°N (COU minus BGC) taking 10-yr means between 1861 and 2100 and perturbations to cumulative CO_2 uptake (PgC) (COU minus BGC) over 45°S – 45°N ; (b) relationship between perturbations to globally averaged surface air temperature ($^{\circ}\text{C}$) (COU minus BGC) ($^{\circ}\text{C}$) and perturbations to cumulative CO_2 uptake (PgC) (COU minus BGC) over 45°S – 45°N ; (c) relationship between perturbations to global atmospheric surface air temperature (TAS) perturbations ($^{\circ}\text{C}$) averaged over 45°S – 45°N (COU minus BGC) taking 10-yr means between 1861 and 2100 and perturbations to SST ($^{\circ}\text{C}$) averaged over 45°S – 45°N (COU minus BGC) taking 10-yr means between 1861 and 2100; (d) relationship between perturbations to cumulative CO_2 uptake (PgC) over 45°S – 45°N and perturbation to spatially integrated surface nDIC ($\mu\text{mol kg}^{-1}$) over 45°S – 45°N .

century. The transition in this sensitivity occurs at approximately 0.8°C . In other words, there is a pronounced nonlinearity in the relationship between large-scale temperature perturbations and large-scale cumulative carbon uptake perturbations. Next cumulative CO_2 uptake perturbations over 45°S – 45°N are considered against globally averaged surface air temperature (Fig. 7b) shows a similar structure, reflecting the close correspondence of SSTs averaged over 45°S – 45°N with globally averaged surface air temperature (Fig. 7c). Taken together, this analysis suggests that the temporal structure of cumulative ocean CO_2 flux perturbations to global surface temperature perturbations presented by Friedlingstein et al. (2006) are reflecting the heat–carbon feedback mechanism with an underlying nonlinear response. Last but not least, the relationship between perturbations to cumulative CO_2

uptake over 45°S – 45°N are shown against changes in the mean nDIC concentrations (COU minus BGC) averaged over 45°S – 45°N (Fig. 7d). This reveals a close correspondence between two fields, but with a similar curvature to what is seen in Fig. 7a.

As a complement to the analysis presented in Fig. 6 for the projected 2090s evolution of $p\text{CO}_2$ in SST–nDIC phase space, we consider in Fig. 8 a similar analysis for the modeled behavior of $p\text{CO}_2$ over the 2000s (specifically a climatology over 2000–09) against two climatologies derived from observations over the same period. In particular, we consider variability over three of the four regions that were presented in Fig. 5, using the interannually varying monthly gridded products of Majkut et al. (2014) (PU-MCMC) and Iida et al. (2015) (JMA). For three of these regions, the modeled evolution

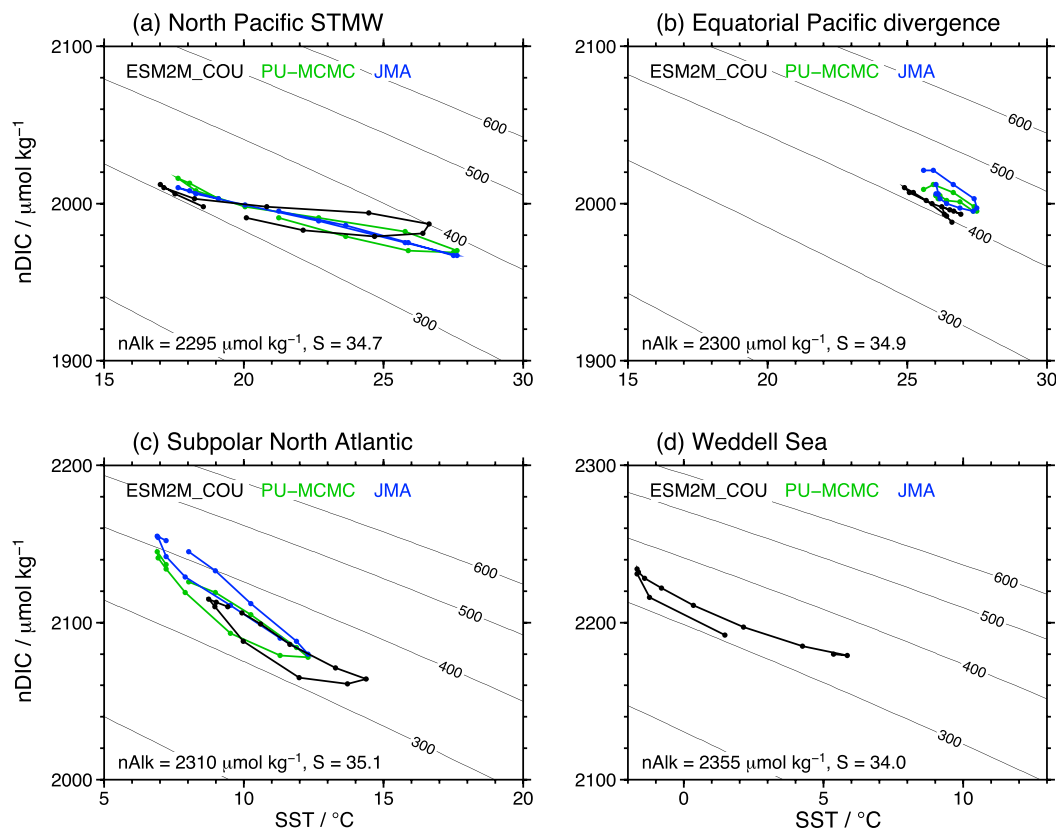


FIG. 8. Phase diagram for $p\text{CO}_2$ evolution SST–nDIC space showing climatological monthly evolution during the 2000s (specifically a climatology over 2000–09) for the same regions considered in Fig. 5. Data constraints are derived from the interannually gridded products of Majkut et al. (2014) (PU-MCMC) and Iida et al. (2015) (JMA). The regions considered are (a) NPSTMW (140° – 160° E, 30° – 35° N), (b) EQDIV (140° – 130° W, 5° S– 5° N), (c) SPNA (40° – 30° W, 50° – 60° N), and (d) WEDD (40° – 30° W, 62° – 72° S). Output from the COU simulation are superposed for comparison. For WEDD data constraints were deemed to not be sufficient to be included, but the model behavior is shown. The figure uses K_0 from Weiss (1974) and K_1 and K_2 from Lueker et al. (2000).

for COU over the 2000s (ESM2M_COU) is evaluated against the observational constraints. Although the ESM2M_COU evolution is also shown for the WEDD region in the 2000s (Fig. 8d), data constraints there were deemed to be insufficient to merit comparison against the modeled state.

For the three cases where the model is explicitly compared with the observations (Figs. 8a–c), the two observational products (PU_MCMC and JMA) are in fact more similar to each other than to the model (ESM2M_COU), supporting our assumption that the observational products are valid for assessing model biases. For the NPSTMW site (Fig. 8a) the analysis indicates that agreement between all three estimates is best in winter, with model biases of order $10 \mu\text{mol kg}^{-1}$ for nDIC and of order 1°C for SST, and biases toward a weak $p\text{CO}_2$ of order 10 – $20 \mu\text{atm}$. Biases in summer are approximately twice as large for this region. For the case of EQDIV (Fig. 8b) the model exhibits a bias with nDIC that is low by 10 – $20 \mu\text{mol kg}^{-1}$, and an annual mean

$p\text{CO}_2$ that is too low by 10 – $40 \mu\text{atm}$, although the amplitude in the seasonal cycle in nDIC and SST well approximates those identified in the observational products. For the subpolar North Atlantic (Fig. 8c) the model reveals a substantial bias (too warm by 2° – 3°C and nDIC concentrations too low by 10 – $30 \mu\text{mol kg}^{-1}$, and $p\text{CO}_2$ in winter (the time of minimum temperatures) is 25 – $50 \mu\text{atm}$ smaller than the observational products. For the Weddell Sea, the evolution of $p\text{CO}_2$ in SST–nDIC phase space is shown for the model for consistency, but as was stated earlier data sparsity issues in these regions render these fields to be inappropriately represented in the PU_MCMC and JMA observationally based products.

4. Discussion

We set out to investigate the degree to which heat and carbon coupling under enhanced anthropogenic carbon emissions can occur through the impact of heat on the

solubility of CO_2 and ensuing perturbations to the CO_2 buffering capacity of seawater under CO_2 invasion, in the absence of perturbations to the physical circulation state or the biological state of the ocean. We began with a global analysis, and we were able to identify that nearly half (48%) of the global ocean carbon–climate feedback occurs over the latitude range 45°S – 45°N for GFDL’s ESM2M, with approximately 60% of the global uptake of anthropogenic CO_2 occurring over this same latitude range. To attribute the degree to which this behavior over 45°S – 45°N is due to solubility effects rather than perturbations to the ventilation or biological state of the ocean, we devised a new simulation (COU_CC) that maintained a preindustrial physical circulation state of the ocean, but includes the impact of climate warming from our COU simulation. This was accomplished through the representation of temperature and salinity in the calculation of $p\text{CO}_2$ exclusively in the gas exchange routines of the model. With this COU_CC simulation, we were able to confirm that it is the impact of warming on solubility, that is enhanced by the diminished buffering capacity of CO_2 in seawater in a high- CO_2 world, rather than changes in ventilation or stratification, that dominate the marine carbon–climate feedbacks over 45°S – 45°N .

The analysis of cumulative carbon perturbations (COU minus BGC) versus SST perturbations (COU minus BGC) over 45°S – 45°N in Fig. 7a illustrated a sensitivity that increases with time, in particular above the 1°C warming perturbation threshold. This delayed response in cumulative CO_2 uptake to warming may well reflect the decadal water mass renewal time scales for the shallow overturning, in particular an intergyre-exchange time scale for thermocline waters that upwell along the equator (Fine et al. 2001). In other words, as the offset of COU from BGC for EQDIV (Fig. 6b) is not a local but rather a delayed response to conditions in the extratropical source regions (upwelling of waters that have had their CO_2 buffering capacity reduced through the invasion flux of CO_2 from the atmosphere) related to the equatorial region through thermocline transport.

To reiterate our principal result, the heat–carbon feedback is triggered over 45°S – 45°N by surface warming, and subsequently the sensitivity of sea surface $p\text{CO}_2$ to further temperature perturbations is amplified by the cumulative invasion flux of C_{ant} and its impact on surface DIC concentrations. It is then important to consider the degree to which the results presented here may be model-specific. One area of concern with ESM2M is that it has been documented to be on the low end of the CMIP5 models in terms of its transient climate sensitivity, meaning that feedbacks could be weaker with this

model than other CMIP5-class models. Even with this model expected to experience a weaker TCR (Forster et al. 2013), including a weaker warming response over the low latitudes, the heat–carbon feedback identified here is nevertheless interpreted to be robust. The question also arises as to whether the model’s temperature bias in summer in Fig. 8a (the North Pacific STMW formation region) complicates our interpretation of the importance of the warm season in sustaining the heat–carbon feedback. There we wish to emphasize that the amplitude of the seasonal cycle in SST in the model has a bias of less than 10%, which is not large. It is in fact the model skill with the seasonal amplitude that is of particular interest for our inferred mechanism. It also warrants mention that the mapping uncertainties for carbon-related variables within observational products are larger than 10%, as is clear from a number of studies (Wanninkhof et al. 2013; Rödenbeck et al. 2015; Gregor et al. 2019), with biases also being large for the seasonal cycle on local scales. We recommend that future work address seasonal biases seen here in ESM2M comprehensively more broadly in CMIP-class models.

Recently there has been interest in evaluating Earth system models to develop emergent constraints to identify clues from historical records to constrain projected future changes in the Earth system (e.g., Cox et al. 2013). It warrants mention here that there is a stark contrast for the equatorial Pacific region between the climatological seasonal changes emphasized in Fig. 6b and the variations of $p\text{CO}_2$ on El Niño time scales for the model (not shown). The amplitude of the climatological seasonal cycle in $p\text{CO}_2$ is small, with displacements in SST–nDIC space largely along the derived stationary $p\text{CO}_2$ isolines, whereas for El Niño–Southern Oscillation (ENSO) time scales the variability is large with important displacements of $p\text{CO}_2$ in SST–nDIC space that are transverse to the derived stationary $p\text{CO}_2$ isolines in the figure. In the language of Takahashi et al. (2002) and Feely et al. (2002), the feedback as manifested in $p\text{CO}_2$ over the EQDIV region (the offset of COU relative to BGC) is SST driven, with this being confirmed over larger scales with the COU_CC simulation shown in Fig. 2. This then stands in contrast to ENSO time scales, where the changes in $p\text{CO}_2$ in the equatorial Pacific upwelling region were identified by Takahashi et al. (2002) and Feely et al. (2002) as being DIC driven (circulation and biology) rather than SST driven. We interpret this to provide a note of caution regarding the consideration of “emergent constraints” as a means to relate observed changes in the modern ocean state to project future changes. Although this has been argued to work for marine net primary productivity (NPP) (Kwiatkowski et al. 2017) and for terrestrial carbon–climate feedbacks (Cox et al. 2013),

the mechanisms controlling carbon feedbacks are distinct here from the mechanisms controlling ENSO variability in sea surface $p\text{CO}_2$.

Although our principal focus in this study has been on the lower latitudes, there are two points with respect to the higher latitudes that warrant mention. First, as we pointed out for the subpolar North Atlantic (Fig. 6c) and the Weddell Sea (Fig. 6d), the offset of the COU and BGC runs relative to the constant $p\text{CO}_2$ isolines in the figures indicates changes that are primarily DIC driven rather than SST driven. In fact, this holds over larger scales, as is revealed for the integrated CO_2 fluxes over the high latitudes (Fig. 2b). There the integrated CO_2 fluxes for COU_CC more closely follow BGC than COU. The second point that we wish to emphasize for the high latitudes is that the feedbacks there may become important after they have become important over the low latitudes. This can be inferred by comparing the degree of separation between COU and BGC over the high latitudes (Fig. 2b) and the low latitudes (Fig. 2c). Resolving this more quantitatively will require a large ensemble approach for both BGC and COU, as a means to distinguish between forced responses and natural variability.

The mechanism emphasized here over the low latitudes is consistent with the connection made between water column temperature perturbations under climate change and carbon–climate feedbacks identified by Schwinger and Tjiputra (2018), albeit with different perturbations applied to different Earth system models. Although well beyond the scope of this study, a constructive path forward may well be to extend the analyses with CMIP5 and CMIP6 models presented by Arora et al. (2020) for which the array of COU and BGC simulations exist with 1% per year atmospheric forcing for quantifying feedbacks by region considered here and in Table 2 of Roy et al. (2011). This will help to resolve the following question: Do CMIP5 models tend to exhibit a stronger low-latitude contribution to global carbon–climate feedbacks than ESM2M (the model considered here), with this reflecting the weak thermal transient climate response found for ESM2M?

The analyses of $p\text{CO}_2$ evolution in SST–nDIC phase space in Figs. 6 and 8 does not in itself reveal whether and how modulations of the seasonal cycle resulting from changes in the CO_2 buffering capacity of seawater may contribute to carbon–climate feedbacks. These results are consistent with the findings of the earlier studies (Rodgers et al. 2008; Riebesell et al. 2009; Gorgues et al. 2010; Hauck and Völker 2015; Landschützer et al. 2018; Fassbender et al. 2018) that have emphasized the growth of the seasonal cycle in sea surface $p\text{CO}_2$ under the joint effects of the invasion flux of C_{ant} and warming. It is left

as a subject for future investigation to explore the degree to which carbon–climate feedbacks over the low latitudes emphasized here are stronger over summer than winter months.

5. Conclusions

Our analysis has identified a heat–carbon feedback mechanism that sustains approximately half of the global carbon–climate feedback by 2100 under historical/RCP8.5 perturbations with GFDL’s ESM2M Earth system model. Over the latitude range 45°S – 45°N , where approximately 60% of the global ocean uptake of anthropogenic carbon (C_{ant}) occurs in ESM2M, the heat–carbon feedback emphasized here is dominant. Importantly, the heat–carbon feedback is distinct from and weaker than what one would expect from the effect of solubility (through surface ocean warming) on $p\text{CO}_2$ alone. Rather, this low-latitude feedback is initially triggered by surface temperature perturbations, but it is then further amplified through the effect of the net cumulative invasion flux of anthropogenic carbon into the surface ocean. This in turn enhances the sensitivity of $p\text{CO}_2$ temperature changes, in particular during summer conditions. As a consequence of less CO_2 uptake by the ocean in a higher CO_2 world, more CO_2 is left in the atmosphere, enhancing further warming.

A rectification of the seasonal cycle in $p\text{CO}_2$ in the subtropics was identified to play an important role in sustaining the heat–carbon feedback identified here. This occurs in particular through enhanced summer outgassing of CO_2 for COU relative to BGC in the subtropics, but also more generally through a modulation of the full seasonal cycle. The fact that seasonal $p\text{CO}_2$ variability in the subtropics is amplified for COU relative to BGC is due to the full invasion flux (COU minus PIN) of C_{ant} , with this overwhelming the much smaller compensation effect seen in Revelle factor differences between COU and BGC. The fact that the feedback over 45°S – 45°N is relatively weak for perturbation temperatures less than 0.8°C , and then increases strongly for temperature perturbations greater than 0.8°C (Fig. 7a) is interpreted to represent a delay associated with the renewal time scales for thermocline waters (Fine et al. 2001). This serves to underscore the importance of reemergence of C_{ant} into the ocean’s mixed layer as a mechanism that can modulate the strength of the heat–carbon feedback.

The introduction of the COU_CC run (invoking data override) provided independent support for our main mechanistic interpretation, namely that the heat–carbon feedback dominates carbon–climate feedbacks over 45°S – 45°N . The experiment confirms that the feedback is triggered by heating and then amplified by the invasion

flux of C_{ant} , rather than being driven by ventilation rate perturbations (circulation state changes) or perturbations to biology over 45°S–45°N. This study complements previous works that have emphasized positive marine carbon–climate feedbacks that are driven by the combined effects of circulation state and biological perturbations over the high latitudes (Maier-Reimer et al. 1996; Sarmiento et al. 1998). It is our hope that this study will motivate future explorations of how the heat and carbon coupling mechanisms discussed here operate over higher latitudes, where there is a more complicated interplay between a broader variety of mechanisms to sustain feedbacks.

Acknowledgments. The contribution of K.B.R. came through IBS-R028-D1. Support for M.I. and K.T. came through MRI's research fund C4 for the study of ocean biogeochemistry and acidification and MEXT KAKENHI Grant 19H05700 (HotSpot2). T.L.F. acknowledges financial support from the Swiss National Science Foundation Grant PP00P2_170687 and the European Union's Horizon 2020 Research and Innovative Programme under Grant Agreement 821003 (4C project). The authors thank Daniele Iudicone and Jorge Sarmiento for fruitful discussions.

REFERENCES

- Anderson, J. L., and Coauthors, 2004: The new GFDL global atmosphere and land model AM2-LM2: Evaluation with prescribed SST simulations. *J. Climate*, **17**, 4641–4673, <https://doi.org/10.1175/JCLI-3223.1>.
- Arora, V. K., and Coauthors, 2020: Carbon-concentration and carbon-climate feedbacks in CMIP6 models, and their comparison to CMIP5 models. *Biogeosciences*, <https://doi.org/10.5194/bg-2019-473>, in press.
- Banks, H. T., and J. M. Gregory, 2006: Mechanisms of ocean heat uptake in a coupled climate model and the implications for tracer based predictions of ocean heat uptake. *Geophys. Res. Lett.*, **33**, L07608, <https://doi.org/10.1029/2005GL025352>.
- Cox, P. M., R. A. Betts, C. D. Jones, S. A. Spall, and I. J. Totterdell, 2000: Acceleration of global warming due to carbon-cycle feedbacks in a coupled climate model. *Nature*, **408**, 184–187, <https://doi.org/10.1038/35041539>.
- , D. Pearson, B. B. Booth, P. Friedlingstein, C. Huntingford, C. D. Jones, and C. M. Luke, 2013: Sensitivity of tropical carbon to climate change constrained by carbon dioxide variability. *Nature*, **494**, 341–344, <https://doi.org/10.1038/nature11882>.
- Cramer, W., and Coauthors, 2001: Global response of terrestrial ecosystem structure and function to CO₂ and climate change: Results from six dynamic global vegetation models. *Global Change Biol.*, **7**, 357–373, <https://doi.org/10.1046/j.1365-2486.2001.00383.x>.
- de Lavergne, C., J. B. Palter, E. D. Galbraith, R. Bernardello, and I. Marinov, 2014: Cessation of deep convection in the open Southern Ocean under anthropogenic climate change. *Nat. Climate Change*, **4**, 278–282, <https://doi.org/10.1038/nclimate2132>.
- Delworth, T. L., and Coauthors, 2006: GFDL's CM2 global coupled climate models, Part I: Formulation and simulation characteristics. *J. Climate*, **19**, 643–674, <https://doi.org/10.1175/JCLI3629.1>.
- Dunne, J. P., and Coauthors, 2012: GFDL's ESM2 global coupled climate–carbon Earth system models. Part I: Physical formulation and baseline simulation characteristics. *J. Climate*, **25**, 6646–6665, <https://doi.org/10.1175/JCLI-D-11-00560.1>.
- , and Coauthors, 2013: GFDL's ESM2 global coupled climate–carbon Earth system models. Part II: Carbon system formulation and baseline simulation characteristics. *J. Climate*, **26**, 2247–2267, <https://doi.org/10.1175/JCLI-D-12-00150.1>.
- , A. Gnanadesikan, J. L. Sarmiento, and R. D. Slater, 2010: Technical description of the prototype version (v0) of Tracers of Phytoplankton with Allometric Zooplankton (TOPAZ) ocean biogeochemical model as used with the Princeton IFMIP model. *Biogeosciences*, **7**, 3593–3624, <https://bg.copernicus.org/articles/7/3593/2010/bg-7-3593-2010-supplement.pdf>.
- Fassbender, A. J., K. B. Rodgers, H. I. Palevsky, and C. L. Sabine, 2018: Seasonal asymmetry in the evolution of surface ocean pCO₂ and pH thermodynamic drivers and the influence on sea-air CO₂ flux. *Global Biogeochem. Cycles*, **32**, 1476–1497, <https://doi.org/10.1029/2017GB005855>.
- Feely, R. A., and Coauthors, 2002: Seasonal and interannual variability of CO₂ in the equatorial Pacific. *Deep-Sea Res. II*, **49**, 2443–2469, [https://doi.org/10.1016/S0967-0645\(02\)00044-9](https://doi.org/10.1016/S0967-0645(02)00044-9).
- Fine, R. A., K. A. Maillet, K. F. Sullivan, and D. Willey, 2001: Circulation and ventilation flux of the Pacific Ocean. *J. Geophys. Res.*, **106**, 22 159–22 178, <https://doi.org/10.1029/1999JC000184>.
- Forster, P. M., T. Andrews, P. Good, J. M. Gregory, L. S. Jackson, and M. Zelinka, 2013: Evaluating adjusted forcing and model spread for historical and future scenarios in the CMIP5 generation of climate models. *J. Geophys. Res. Atmos.*, **118**, 1139–1550, <https://doi.org/10.1002/jgrd.50174>.
- Friedlingstein, P., J.-L. Dufresne, P. M. Cox, and P. Rayner, 2003: How positive is the feedbacks between climate change and the carbon cycle? *Tellus*, **55B**, 692–700, <https://doi.org/10.3402/tellusb.v55i2.16765>.
- , and Coauthors, 2006: Climate–carbon cycle feedback analysis: Results from the C4MIP-Model Intercomparison. *J. Climate*, **19**, 3337–3353, <https://doi.org/10.1175/JCLI3800.1>.
- , and Coauthors, 2019: Global carbon budget 2019. *Earth Syst. Sci. Data*, **11**, 1783–1838, <https://doi.org/10.5194/essd-11-1783-2019>.
- Frölicher, T., J. Sarmiento, D. Payntner, J. Dunne, J. Krasting, and M. Winton, 2015: Dominance of the Southern Ocean in anthropogenic carbon and heat uptake in CMIP5 models. *J. Climate*, **28**, 862–886, <https://doi.org/10.1175/JCLI-D-14-00117.1>.
- Goodman, P. J., W. Hazeleger, P. de Vries, and M. Cane, 2005: Pathways into the Pacific Equatorial Undercurrent: A trajectory analysis. *J. Phys. Oceanogr.*, **35**, 2134–2151, <https://doi.org/10.1175/JPO2825.1>.
- Gorgues, T., O. Aumont, and K. B. Rodgers, 2010: A mechanistic account of increasing seasonal variations in the rate of ocean uptake of anthropogenic carbon. *Biogeosciences*, **7**, 2581–2589, <https://doi.org/10.5194/bg-7-2581-2010>.
- Gregor, L., A. D. Lebehoh, S. Kok, and P. M. S. Monteiro, 2019: A comparative assessment of the uncertainties of global surface ocean CO₂ estimates using a machine-learning ensemble (CSIR-ML6 version 2019a)—Have we hit the wall? *Geosci. Model Dev.*, **12**, 5113–5136, <https://doi.org/10.5194/gmd-12-5113-2019>.
- Gregory, J. M., C. D. Jones, P. Cadule, and P. Friedlingstein, 2009: Quantifying carbon cycle feedbacks. *J. Climate*, **22**, 5232–5250, <https://doi.org/10.1175/2009JCLI2949.1>.
- Griffies, S. M., 2009: Elements of MOM4p1. GFDL Ocean Group Tech. Rep. 6, accessed 16 May 2011, 431 pp.,

- https://www.gfdl.noaa.gov/wp-content/uploads/files/model_development/ocean/guide4p1.pdf.
- Hauck, J., and C. Völker, 2015: Rising atmospheric CO₂ leads to large impact of biology on Southern Ocean CO₂ uptake via changes of the Revelle factor. *Geophys. Res. Lett.*, **42**, 1459–1464, <https://doi.org/10.1002/2015GL063070>.
- Iida, Y., A. Kojima, Y. Takatani, T. Nakano, H. Sugimoto, T. Midorikawa, and M. Ishii, 2015: Trends in pCO₂ and sea-air CO₂ flux over the global open oceans for the last two decades. *J. Oceanogr.*, **71**, 637–661, <https://doi.org/10.1007/s10872-015-0306-4>.
- Iudicone, D., K. B. Rodgers, Y. Plancherel, O. Aumont, T. Ito, R. M. Key, G. Madec, and M. Ishii, 2016: The formation of the ocean's anthropogenic carbon reservoir. *Sci. Rep.*, **6**, 35473, <https://doi.org/10.1038/srep35473>.
- Joos, F., G.-K. Plattner, T. F. Stocker, O. Marchal, and A. Schmittner, 1999: Global warming and marine carbon cycle feedbacks on future atmospheric CO₂. *Science*, **284**, 464–467, <https://doi.org/10.1126/science.284.5413.464>.
- Kurihara, Y., T. Sakurai, and T. Kuragano, 2006: Global daily sea surface temperature analysis using data from satellite microwave radiometer, satellite infrared radiometer and in situ observations (in Japanese). *Sokko-Jiho*, **73**, S1–S18.
- Kwiatkowski, L., L. Bopp, O. Aumont, P. Ciais, P. M. Cox, C. Laufkötter, Y. Li, and R. Séférian, 2017: Emergent constraints on projections of declining primary production in the tropical oceans. *Nat. Climate Change*, **7**, 355–358, <https://doi.org/10.1038/nclimate3265>.
- Landschützer, P., N. Gruber, D. C. E. Bakker, I. Stemmler, and K. D. Six, 2018: Strengthening seasonal marine CO₂ variations due to increasing atmospheric CO₂. *Nat. Climate Change*, **8**, 146–150, <https://doi.org/10.1038/s41558-017-0057-x>.
- Lee, K., and Coauthors, 2006: Global relationships of total alkalinity with salinity and temperature in surface waters in the world's oceans. *Geophys. Res. Lett.*, **33**, L19605, <https://doi.org/10.1029/2006GL027207>.
- Lueker, T. J., A. G. Dickson, and C. D. Keeling, 2000: Ocean pCO₂ calculated from dissolved inorganic carbon, alkalinity, and equations for K₁ and K₂: Validation based on laboratory measurements of CO₂ in gas and seawater at equilibrium. *Mar. Chem.*, **70**, 105–119, [https://doi.org/10.1016/S0304-4203\(00\)00022-0](https://doi.org/10.1016/S0304-4203(00)00022-0).
- Maier-Reimer, E., U. Mikolajewicz, and A. Winguth, 1996: Future ocean uptake of CO₂: Interaction between ocean circulation and biology. *Climate Dyn.*, **12**, 711–722, <https://doi.org/10.1007/s003820050138>.
- Majkut, J. D., J. L. Sarmiento, and K. B. Rodgers, 2014: A growing oceanic carbon uptake: Results from an inversion study of surface pCO₂ data. *Global Biogeochem. Cycles*, **28**, 335–351, <https://doi.org/10.1002/2013GB004585>.
- Manabe, S., R. J. Stouffer, M. J. Spelman, and K. Bryan, 1991: Transient responses of a coupled ocean–atmosphere model to gradual changes of atmospheric CO₂. Part I: Annual mean response. *J. Climate*, **4**, 785–818, [https://doi.org/10.1175/1520-0442\(1991\)004<0785:TROACO>2.0.CO;2](https://doi.org/10.1175/1520-0442(1991)004<0785:TROACO>2.0.CO;2).
- Mehrbach, C., C. H. Culberso, J. E. Hawley, and R. M. Pytkowicz, 1973: Measurement of the apparent dissociation constants of carbonic acid in seawater at atmospheric pressure. *Limnol. Oceanogr.*, **18**, 897–907, <https://doi.org/10.4319/lo.1973.18.6.0897>.
- Najjar, R. G., and J. C. Orr, 1999: Biotic-HOWTO. OCMIP Internal Rep., 15 pp., <http://www.cgd.ucar.edu/oce/OCMIP/HOWTO-Biotic.pdf>.
- Nakano, H., M. Ishii, K. B. Rodgers, H. Tsujino, and G. Yamanaka, 2015: Anthropogenic CO₂ uptake, transport, storage, and dynamical controls in the ocean imposed by the meridional overturning circulation: A modeling study. *Global Biogeochem. Cycles*, **29**, 1706–1724, <https://doi.org/10.1002/2015GB005128>.
- Nakićenović, N., and R. Swart, Eds., 2000: *Special Report on Emissions Scenarios*. Cambridge University Press, 599 pp.
- Revelle, R., and H. E. Suess, 1957: Carbon dioxide exchange between atmosphere and ocean and the question of an increase of atmospheric CO₂ during the past decades. *Tellus*, **9**, 18–27, <https://doi.org/10.1111/J.2153-3490.1957.TB01849.X>.
- Riebesell, U., A. Körtzinger, and A. Oschlies, 2009: Sensitivities of marine carbon fluxes to ocean change. *Proc. Natl. Acad. Sci. USA*, **106**, 20 602–20 609, <https://doi.org/10.1073/pnas.0813291106>.
- Rödenbeck, C., and Coauthors, 2015: Data-based estimates of ocean carbon sink variability—The first results of the Surface Ocean pCO₂ Mapping intercomparison (SOCOM). *Biogeosciences*, **12**, 7251–7278, <https://doi.org/10.5194/bg-12-7251-2015>.
- Rodgers, K. B., B. Blanke, G. Madec, O. Aumont, P. Ciais, and J. C. Dutay, 2003: Extratropical sources of equatorial Pacific upwelling in an OGCM. *Geophys. Res. Lett.*, **30**, 1084, <https://doi.org/10.1029/2002GL016003>.
- , J. L. Sarmiento, O. Aumont, C. Crevoisier, C. de Boyer Montégut, and N. Metzl, 2008: A wintertime uptake window for anthropogenic CO₂ in the North Pacific. *Global Biogeochem. Cycles*, **22**, GB2020, <https://doi.org/10.1029/2006GB002920>.
- , J. Lin, and T. L. Frölicher, 2015: Emergence of multiple ocean ecosystem drivers in a large ensemble suite with an Earth system model. *Biogeosciences*, **12**, 3301–3320, <https://doi.org/10.5194/bg-12-3301-2015>.
- Roy, T., and Coauthors, 2011: Regional impacts of climate change and atmospheric CO₂ on future ocean carbon uptake: A multimodel linear feedback analysis. *J. Climate*, **24**, 2300–2318, <https://doi.org/10.1175/2010JCLI3787.1>.
- Sarmiento, J., T. Hughes, R. Stouffer, and S. Manabe, 1998: Simulated response of the ocean carbon cycle to anthropogenic climate warming. *Nature*, **393**, 245–249, <https://doi.org/10.1038/30455>.
- Schlunegger, S., K. B. Rodgers, J. L. Sarmiento, and T. L. Frölicher, J. P. Dunne, M. Ishii, and R. Slater, 2019: Emergence of anthropogenic signals in the ocean carbon cycle. *Nat. Climate Change*, **9**, 719–725, <https://doi.org/10.1038/s41558-019-0553-2>.
- Schwinger, J., and J. F. Tjiputra, 2018: Ocean carbon cycle feedbacks under negative emissions. *Geophys. Res. Lett.*, **45**, 5062–5070, <https://doi.org/10.1029/2018GL077790>.
- , and Coauthors, 2014: Nonlinearity of ocean carbon cycle feedbacks in CMIP5 Earth system models. *J. Climate*, **27**, 3869–3888, <https://doi.org/10.1175/JCLI-D-13-00452.1>.
- Siegenthaler, U., and H. Oeschger, 1978: Predicting future atmospheric carbon dioxide levels. *Science*, **199**, 388–395, <https://doi.org/10.1126/science.199.4327.388>.
- Takahashi, T., and Coauthors, 2002: Global sea-air CO₂ flux based on climatological surface ocean pCO₂, and seasonal biological temperature effects. *Deep-Sea Res. II*, **49**, 1601–1622, [https://doi.org/10.1016/S0967-0645\(02\)00003-6](https://doi.org/10.1016/S0967-0645(02)00003-6).
- Takatani, Y., and Coauthors, 2014: Relationships between total alkalinity in surface water and sea surface dynamic height in the Pacific Ocean. *J. Geophys. Res. Oceans*, **119**, 2806–2814, <https://doi.org/10.1002/2013JC009739>.
- Toyama, K., K. B. Rodgers, B. Blanke, D. Iudicone, M. Ishii, O. Aumont, and J. L. Sarmiento, 2017: Large reemergence of anthropogenic carbon into the ocean's surface mixed layer sustained by the ocean's overturning circulation. *J. Climate*, **30**, 8615–8631, <https://doi.org/10.1175/JCLI-D-16-0725.1>.
- Usui, N., S. Ishizaki, Y. Fujii, H. Tsujino, T. Yasuda, and M. Kamachi, 2006: Meteorological Research Institute Multivariate Ocean

- Variational Estimation (MOVE) system: Some early results. *Adv. Space Res.*, **37**, 806–822, <https://doi.org/10.1016/j.asr.2005.09.022>.
- Van Heuven, S., D. Pierrot, J. W. B. Rae, E. Lewis, and D. W. R. Wallace, 2011: MATLAB program developed for CO₂ system calculations. ORNL/CDIAC-105b, Carbon Dioxide Information Analysis Center, Oak Ridge National Laboratory, https://doi.org/10.3334/CDIAC/otg.CO2SYS_MATLAB_v1.1.
- van Vuuren, D. P., and Coauthors, 2011: The representative concentration pathways: An overview. *Climatic Change*, **109**, 5, <https://doi.org/10.1007/s10584-011-0148-z>.
- Wanninkhof, R., and Coauthors, 2013: Global ocean carbon uptake: Magnitude, variability, and trends. *Biogeosciences*, **10**, 1983–2000, <https://doi.org/10.5194/bg-10-1983-2013>.
- Weiss, R.F., 1974: Carbon dioxide in water and seawater: The solubility of a non-ideal gas. *Mar. Chem.*, **2**, 203–215, [https://doi.org/10.1016/0304-4203\(74\)90015-2](https://doi.org/10.1016/0304-4203(74)90015-2).
- , R. A. Jahnke, and C. D. Keeling, 1982: Seasonal effects of temperature and salinity on the partial pressure of CO₂ in seawater. *Nature*, **300**, 511–513, <https://doi.org/10.1038/300511a0>.
- Winton, M., S. M. Griffies, B. L. Samuels, J. L. Sarmiento, and T. L. Frölicher, 2013: Connecting changing ocean circulation with changing climate. *J. Climate*, **26**, 2268–2278, <https://doi.org/10.1175/JCLI-D-12-00296.1>.
- Xie, P., and G. K. Vallis, 2012: The passive and active nature of ocean heat uptake in idealized climate change experiments. *Climate Dyn.*, **38**, 667–684, <https://doi.org/10.1007/s00382-011-1063-8>.
- Zeebe, R. E., and D. Wolf-Gladrow, 2001: *CO₂ in Seawater: Equilibrium, Kinetics, Isotopes*. Elsevier Oceanography Series, Vol. 65, Elsevier, 346 pp.
- Zhai, P., K. B. Rodgers, S. M. Griffies, R. D. Slater, D. Iudicone, J. L. Sarmiento, and L. Resplandy, 2017: Mechanistic drivers of re-emergence of anthropogenic carbon in the equatorial Pacific. *Geophys. Res. Lett.*, **44**, 9433–9439, <https://doi.org/10.1002/2017GL073758>.